

# Modeling, Design, and Control of the Rehab-Exos, a Joint Torque Controlled Upper-Limb Exoskeleton

Domenico Chiaradia\*, Massimiliano Solazzi\*, Rocco Vertechy†, and Antonio Frisoli\*

**Abstract**—In the last two decades, the research on exoskeletons has been increasing for several applications. The mechanical architecture of the exoskeleton directly influences its performances in terms of torque and position control. Another aspect is the complexity of the joint design and the number of the required actuators and sensors per joint. In this work we present an upper-limb exoskeleton designed with compact elastic joints with torque sensors based on strain gauges. The torque sensor performances and the design aspects that affect the unwanted non-axial moment load crosstalk are addressed in this study. The joints have a high reduction ratio and they display an output torque of 150 Nm, nevertheless, they are transparent by control and show a low error in both haptic force rendering and position control. Good transparency and force rendering are obtained by model-based full-state feedback control. The control schema takes into account part of the torque sensor non-linearities. Performances have been evaluated using different controls showing that this solution is a valid trade-off among exoskeleton complexity, maximum torque, transparency, and haptic capabilities.

**Index Terms**—Joint torque sensor, elastic joint, upper-limb exoskeleton, full-state feedback control, transparency, haptic rendering

## I. INTRODUCTION

Exoskeletons are robotic interfaces for human-robot interaction where the highest physical symbiosis with the human operator is achieved. Unlike many industrial robots designed to exhibit a stiff structure and therefore to be used with a rigid position control, the exoskeletons are in direct contact with humans, so that they have to satisfy safety and compliance requirements. In the last two decades, several exoskeleton solutions have been proposed using different implementation principles accordingly to the field of application. Some important applications of the exoskeletons are post-stroke neurorehabilitation [1], [2], assistance for limb movements, human power augmentation for lifting heavy loads [3] and teleoperation [4], [5] to enhance the master immersivity and dexterity.

In human-robot interaction devices, different actuation systems and technologies have been exploited. Technologies based on geared solutions [6], [7], [8], tendon drives [9], [10], hybrid solutions (screw and cable actuators) [11] and on pneumatic or hydraulic actuation [12], [13] can be found in literature.

\*D. Chiaradia, M. Solazzi and A. Frisoli are with the PERCRO Laboratory, TeCIP Institute, Scuola Superiore Sant'Anna, Pisa, Italy. E-mail: d.chiaradia@santannapisa.it.

†R. Vertechy is with the DIN-Department of Industrial Engineering University of Bologna, Bologna, Italy. E-mail: rocco.vertechy@unibo.it.

Manuscript received xxx.yy,2018; revised xxx.yy,2018

However in human-robot interaction applications, a fundamental characteristic of the actuation systems is its compliance. The actuators found in recent exoskeletons and humanoids can be classified accordingly to [14] in two main categories: variable impedance actuators (VIA), and stiff actuators suitable for position control strategies. For HRI the use of purely position controlled solution is of limited interest. On the other hand, a variable impedance can be obtained by control (called active impedance by control) or can be a mechanical property, also defined passive impedance (inherent compliance or inherent damping). Figure 1 shows a scheme of the two variable impedance typologies.

In inherent compliance systems an electric motor is coupled with a spring with fixed (Series Elastic Actuator - SEA) or variable stiffness (Variable Stiffness Actuators - VSA). Inherent damping systems are based on the control of the friction by means of eddy currents, controlled rheology or fluid dynamic. Recently double actuation architectures have been developed for variable impedance actuators [15], coupling the stiff motor in parallel with the elastic element (Parallel Elastic Actuators - PEA). Both SEA and VSA have been implemented in exoskeleton as for example in Lopes [16], an exoskeleton for the gait assistance that is based on SEA actuation, or in NEUROexos elbow exoskeleton [17] that is based on VSA and in ALTACRO locomotion exoskeleton [18] that introduces a Mechanically Adjustable Compliance and Controllable Equilibrium Position Actuator (MACCEPA).

All the variable impedance actuators have the advantage of absorbing impacts and SEA, PEA, and VSA (inherent compliance) can eventually mechanically store energy during passive phases and release it in active phases of the movement cycle. In general, adding a series elastic element reduces the peak power demand on the motor. VSAs generally use two motors which increases the size, weight, and complexity of the actuator in comparison with an SEA [19].

On the other side, active impedance systems are electric motors coupled with a transmission/reduction system; they can be classified according to the backdrivability and sensing system. Force controlled actuators implement a force/torque sensor in the joint and can achieve impedance behavior by closed-loop control. In general traditional actuators, due to the absence of elastic or damping elements, can be lighter and more compact than passive variable impedance actuators, but their time response and dynamic bandwidth is limited by control and electrical properties of actuators, such as maximum velocity of electrical motors.

Solutions based on joint torque sensors have been proposed in the last years mostly for lower limb exoskeletons. In [20]

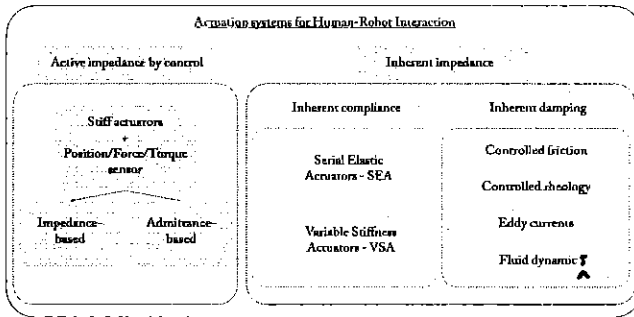


Fig. 1. Schema of variable impedance actuation systems for human-robot interaction. The impedance can be simulated and actively changed by control (this relies on position and torque sensors) or can be an inherent mechanical property of the actuator. In the latter case the mechanical stiffness can be a fixed value (SEA) or can be adjusted (VSA), and the damping can be controlled.

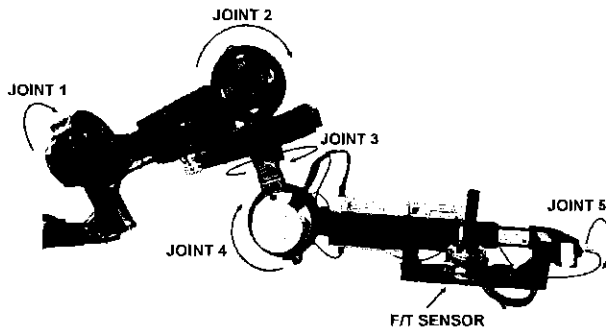


Fig. 2. The Rehab-Exos. It is a 5 DOF upper-limb exoskeleton with 4 actuated joints. The joints  $J_1$ ,  $J_2$  and  $J_4$  share the same characteristics: high reduction ratio (100:1) by means of harmonic drive, embedded torque sensor and maximum actuation torque of 150 Nm. The joint  $J_3$  is composed by a semi-circular guide actuated by a DC motor through tendon transmission. Joint  $J_5$  is passive and the exoskeleton is equipped of a force/torque sensor at the end-effector that is used for evaluation purposes.

and in [21] two knee exoskeletons based on joint torque sensors were presented; the latter exoskeleton implements an admittance control based on the torque sensor reads. In [22] the torque sensor for a lower limb exoskeleton allows to accurately estimate the human muscular torque that were exerted during the human-robot interaction. The advantage of joint torque sensor based solutions is their compactness and robustness, but when the torque sensor is embedded in the joint it is sensitive to the link inertia in addition to the human interaction torques, thus affecting the system transparency. A mechanical solution is presented in [23] where the transparency of a lower-limb exoskeleton has been improved by positioning the force/torque sensor on the supporting cuffs, that is at the interaction point between the human leg and the exoskeleton.

Even if SEA and VSA are less compact than traditional actuators, for example [24] proposed a solution based on a VSA for an exoskeleton of the leg that reduced the lateral size and integrates a torque sensor based on spring's deflection reads. Sensors used to measure these deflections are generally encoders [25] and potentiometers [26]; the latter usually require custom mechanical supports to avoid errors related

with its sensitivity to misalignments. While the deflection based force estimation becomes a most widely utilized method for the SEAs and VSAs and performs fidelity force control performance in various robotic applications, there are still difficulties because of the practical issues such as spring deflection measurement error or noise of the encoder signal [27]. These factors have much negative impact on SEA with high stiffness. In [28], for example, a polymer optical fiber has been mounted on the torsional spring of a SEA to read angles and torques in a more accurate way without considerably enlarging the size of the actuator at the cost of more specific system electronics.

Thus, the use of inherent compliant actuation systems rather than achieving compliance by control systems is not a trivial choice and it depends on the desired mechanical features and is the result of a trade-off among compactness, weight, simplicity, cost, safety, efficiency, and compliance. A good trade-off that prefers compactness, simplicity, and uses just one motor is an active impedance by control actuation system that integrates an elastic component to transmit and to measure axial torques at the same time.

In this paper we address the issue of a collaborative robot behavior by designing an upper limb exoskeleton based on joint torque actuators endowing joint torque sensors and extend our previously work presented in [29]. The Rehab-Exos allows to obtain a physical interaction characterized by good transparency and force rendering accuracy, it is capable to exert a wide range of forces, and at the same time it exhibits high position accuracy due to high gear reduction ratio.

The first part of the paper widely treats the critical issue due to the use of a torque sensor embedded in the joint and in particular the sensitivity to non-axial load has been studied. Then, in the second part the joint model and the control technique are presented.

In particular, regarding transparency we propose an interaction torque control that takes into account the multi-dof non-linear system dynamics and provides a compensation of non-linear effects such as inertial and gravity components, to achieve an accurate estimation of human interaction force. This is accomplished by a single joint optimum observer that ensures joint torque tracking, while a centralized control estimates and compensates for the dynamics of the whole system. Moreover, we have evaluated the effect of dynamic compensation on system transparency highlighting good results.

To validate the proposed control as well as the chosen mechanical architecture, the full-state feedback control has been compared with a basic feedback control and a passivity-based feedback control in two tasks: the zero desired force and the contact with a virtual stiff flat surface. For what concerns haptic rendering, we evaluate at geometrical level the quantitative and qualitative behavior of the proposed controller and we compared it with the other two implemented controllers. Results reward the chosen mechanical and control strategy as presented in the last part of this paper.

This paper is structured as follows: Section II presents the design of the Rehab-Exos with a particular focus on the strain gauge-based torque sensor design and issues. Section III-A

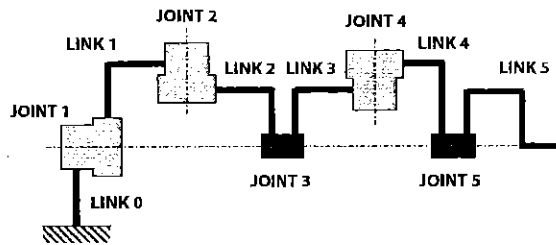


Fig. 3. A schematic representation of the Rehab-Exos exoskeleton.

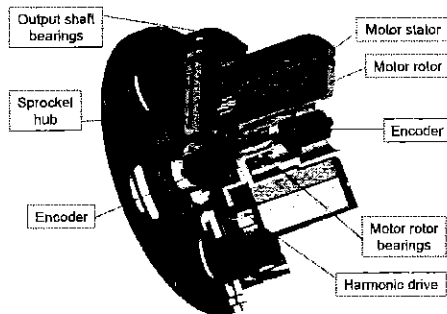


Fig. 4. CAD section of the  $J_1$ ,  $J_2$  and  $J_4$  joint actuator of the Rehab-Exos.

provides a mathematical model of the single joint whereas in the Section III-B the full dynamic model of the Rehab-Exos is described. Section IV explains the proposed full state feedback controller and recalls two torque controls already known in literature. Section V presents the experiments and the obtained results. Finally, discussions and conclusions are addressed in Sections VI and VII, respectively.

## II. SYSTEM DESIGN

The Rehab-Exos is an active robotic exoskeleton (Fig. 2) which is designed with the idea to be compact, easily reconfigurable and to have a good trade-off between transparency and force replication. It was conceived for rehabilitation applications and it is designed in such a way to generate controlled contact forces/torques not only at its end-link handle, but also at intermediate links. When the user is wearing the device he can control the full force interaction with the exoskeleton and guide/be guided involving all articulations of the arm (wrist, shoulder, elbow). The physical interaction between user and exoskeleton is monitored by the joint torque sensors, which performances depend on several design and implementation aspects that are addressed in subsection II-B.

### A. Mechanical design of the Rehab-Exos

As depicted in Fig. 2 and in Fig. 3, the exoskeleton has a serial architecture isomorphic with the human kinematics that comprises: a shoulder joint fixed in space and composed by three active joints  $J_1$ ,  $J_2$  and  $J_3$ ; an active elbow joint  $J_4$ ; and a passive revolute joint  $J_5$  allowing for wrist pronosupination. For a more detailed description of both Rehab-Exos and actuation groups, the reader can refer to [7].

TABLE I  
CHARACTERISTIC DIMENSIONS OF THE TORQUE SENSOR

Dimension	Value [mm]
R	78
r	38
L	24
a	4
round radius	2

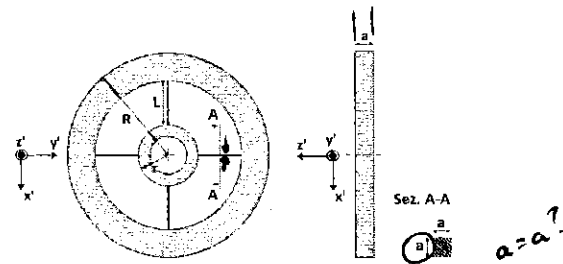


Fig. 5. Characteristic dimensions of the torque sensor.

The three joints  $J_1$ ,  $J_2$  and  $J_4$  of the exoskeleton are motorized through identical actuation groups. Each joint features a custom-made frameless brushless torque motor integrating a compact Harmonic Drive (HD) component set. The actuator provides a joint output torque equal to 150 Nm with an overall weight equal to 3.7 Kg and a motor shaft inertia reduced to the joint output shaft  $J_m = 3.7 \text{ Kg m}^2$ . The Harmonic Drive performs a reduction equal to 100:1. Due to the adopted mechanical components, the joints feature limited back-drivability at motor power-off and limited mechanical complexity to ease maintenance as well as reduce costs. A CAD section of the  $J_1$ ,  $J_2$  and  $J_4$  joints is depicted in Fig. 4. Joint  $J_3$  is characterized by a tendon transmission that is used to transmit the actuation torque through an open semi-circular guide. More detail on the joint  $J_3$  can be found in [7].

### B. Design aspects of the strain gauge based torque sensor

The three joints  $J_1$ ,  $J_2$  and  $J_4$  have a torque sensor featuring a four-spoke-shape geometry. Despite further augmenting the actuation group compliance, the availability of joint-torque sensors enables for multi-contact force control at multiple points distributed over the links and, additionally, makes it possible: 1) to close a stable high-bandwidth torque inner loop around each joint which is weakly affected by robot link variable inertia; 2) to suppress robot vibrations produced by the inherent transmission compliance (Harmonic Drive); 3) to reduce internal disturbance torques caused by actuator and reducer (for instance friction losses, actuator's torque ripples and gear teeth wedging actions); to measure externally applied forces/moments and complex non-linear dynamic interactions between joints and links.

The sensor consists of two fully balanced strain gauge bridges placed on different beams of the spoke, which is located at the joint output shaft. The sensor is made by AISI 630 steel, a harmonic steel exhibiting yield strength of 1950 MPa, Young's modulus of 196 GPa and has been

TABLE II  
STRAIN OF THE 4 STRAIN GAUGES

Probe 1 [m]	Probe 2 [m]	Probe 3 [m]	Probe 4 [m]
1.65e-5	-1.33e-5	-1.91e-5	2.2546e-5

dimensioned to exhibit low weight and high sensitivity to axial moments. The axial torsional stiffness of the sensor is  $k_s = 30 \text{ kNm/rad}$  and can be calculated as in (1).

$$k_s = \frac{\tau}{\theta} = \frac{Ea^4(r + L(1 - Q))}{3L^2(1/2 - Q)} \quad (1)$$

where the adimensional parameter  $Q$  is given by

$$Q = \frac{3r + L}{6r + 3L} \quad (2)$$

where, according to Fig. 5,  $R$  is the radius of the external sensor ring,  $r$  is the radius of the internal sensor ring,  $L$  is length of the beams and  $a$  is the side length of the beam section. The characteristic dimensions of the sensor are reported in TABLE I. Moreover, the overall joint torsional stiffness reduced to the joint output shaft is  $k = 11.38 \text{ kNm/rad}$ .

The position of the strain gauges on the beam is a trade-off: if they were positioned in the middle of the beam the sensor sensitivity would be low, on the contrary, if they were positioned near the extremities the sensor reads would be affected by the non-linearities of the rounds of the beam. The selected distance from the extremities was  $p = 1/8 L = 3 \text{ mm}$ . To estimate the strain of the beam in a given point with distance  $p$  from the inner ring under a certain axial torque  $\tau$ , the normal tension  $\sigma_p$  that acts on that point  $p$  needs to be computed as

$$\sigma_p = \frac{3\tau((1 - Q)L - p)}{2a^3((1 - Q)L + r)} \quad (3)$$

and then the strain follow as

$$\epsilon_A = \frac{\sigma}{E} \quad (4)$$

where  $E$  is the Young's modulus.

Theoretically, i.e. using (4), at  $3 \text{ mm}$  from the inner ring and under an axial torque of  $120 \text{ Nm}$ , a maximum strain of  $2.7 \cdot 10^{-3} \text{ m}$  is obtained. The same test has been conducted using a FEM software tool (Ansys®) because the surface of the strain gauge is not negligible compared to the beam one (see Fig. 8) obtaining a maximum strain of  $1.98 \cdot 10^{-3} \text{ m}$ . The strain of each strain gauge when a  $1 \text{ Nm}$  load is applied can be shown in TABLE II.

An important characteristic of the torque sensor is the sensitivity to non-axial moments, thus an experimental test has been conducted to compute the sensitivity, i.e. a predetermined non-axial torque has been exerted on the sensor in 4 configurations (angle) of the sensor. Experimental results are reported in TABLE III and the sensitivity is equal to

$$S_S = \frac{C_{mis}}{C_S} = 0.067 \quad (5)$$

The sensitivity to non-axial moments is relatively high compared to one mentioned in [30].

TABLE III  
SENSOR READS TO NON-AXIAL MOMENTS

Applied Torque [Nm]	Sensor reads per angle [Nm]			
	0°	45°	90°	180°
32	1.6	2.4	2.2	2.3
64	2.9	4.8	4.4	4.4
96	4.5	7.5	6.9	6.9

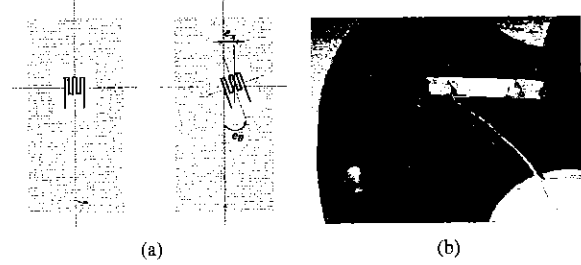


Fig. 6. A possible cause of high sensitivity to non-axial load is the strain gauges's mounting misalignment. The linear displacement  $e_x$  and the angular one  $e_\theta$  are highlighted in (a). A detail of the mounted strain gauges on the torque sensor in (b).

The reason of these results has been investigated and two causes (or a combination of them) have been proposed. The first cause of error could be a strain gauge's mounting misalignment. The second cause could be an excessive deformation of the sensor due to the non-axial moments. About the first hypothesis, the sensitivity of the strain gauges to non-axial load  $C_S$  (when a flexible model of the HD is considered) due to strain gauge's misalignment can be modeled as

$$S_{misal} = k_s \cdot (k_{ex} \cdot e_x + k_{e\theta} \cdot e_\theta) \quad (6)$$

where  $k_s$  is a scaling factor equal to  $7.87e^{-3}$ ,  $k_{ex}$  is the sensitivity to linear mounting misalignment equal to 3,  $k_{e\theta}$  is the sensitivity to angular mounting misalignment equal to 2.3, whereas  $e_x$  and  $e_\theta$  are the positional and angular misalignment errors respectively (see Fig. 6(a)). Equation (6) and the measured sensitivity of 0.067 lead to a misalignment error of millimeters and decades of degree, but these values are over the actual misalignment the installation operator may have introduced as can be seen in Fig. 6(b).

About the second hypothesis it is worth to notice that the sensor from a structural point of view is in series to the HD and this series is in parallel with a couple of bearings. This parallel chain composes a hyper-static system (see Fig. 7), therefore the excessive sensitivity may be due to mounting misalignment of the mechanical parts of the chain.

For the study of the hyper-static system a linear elastic behavior of the system parts were supposed and the system response at non-axial moments was modeled as a mono-dimensional model as in Fig. 7(b). The overall joint stiffness to non-axial moments  $K_{TOT}$  was experimentally evaluated, whereas the non-axial moment stiffness of the torque sensor  $K_{TS}$  and of the HD  $K_{HD}$  were computed via FEM analysis. The FEM results are depicted in Fig. 8 and the stiffness values are reported in table TABLE IV.

should there be values given here?



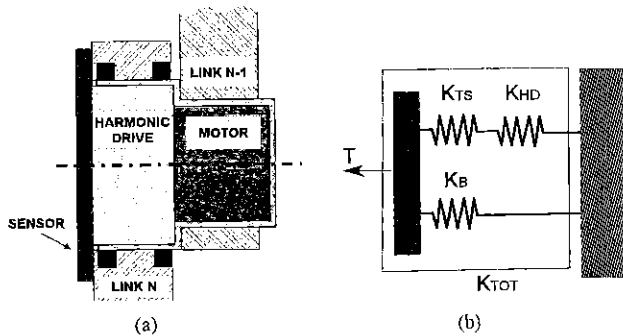


Fig. 7. In a), the schematic representation of the joint. The torque sensor is a series elastic element between the motor and the link n. The torque sensor is not structural and has been designed to transmit only axial torque. In b), the kinematic chain of the joint to non-axial loads.  $K_{TS}$  and  $K_{HD}$  are the stiffness of the torque sensor and of the Harmonic Drive to non-axial load respectively, whereas  $K_B$  is the bearing stiffness.

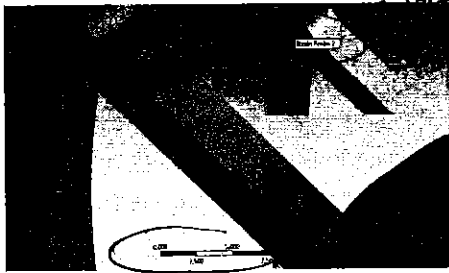


Fig. 8. For the FEM analysis a more dense grid mesh for the zone of interest has been used. For each area the average strain along the radial direction has been computed.

A possible mounting misalignment of the hyper-static chain may be a collinear and/or concentric mounting misalignment between the sensor axis and the bearing axis. In this case, the HD works as a universal joint that connects the sensor (that is connected to the  $(n+1)$ -th link) and the  $n$ -th link. The sensitivity to non-axial moments defined in equation (5) and the mechanical properties in TABLE IV lead to a theoretical mounting misalignment of about 0.5 mm, but this value is not in agreement with the design tolerances and components data-sheets from which a misalignment of about 0.05 mm results in the worst case.

To summarize, unwanted sensor reads to non-axial load may be due to the combination of effects from sensor mounting misalignments and HD excessive deformation.

In order to minimize this undesired effect the authors propose a method based on artificial neural networks (ANN) to characterize and compensate this non-linear behavior that

TABLE IV  
STIFFNESS OF THE COMPONENTS

Component	Stiffness [kNm/rad]
$K_{TS}$	4.1
$K_{HD}$	0.4
$K_B$	23.6
$K_{TOT}$	24

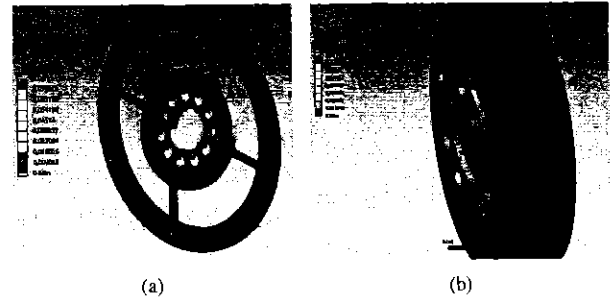


Fig. 9. The FEM analysis results of the torque sensor (a) and of the flexible spline (b) deformation under non-axial load.

results difficult to model. Considering the ideal and linear sensor, the torque readings can be expressed as  $\tau_s = k_v * v$ , where  $v$  is the measured voltage tension and  $k_v$  is the torque sensor's voltage constant. In the real case it can be written  $\hat{\tau}_s = k_v * v + \delta\tau$ , where  $\delta\tau$  is the non-linear influence on the sensor readings due to the mounting and non-axial loads. By experimental evidence, it's possible to assert that the term  $\delta\tau$  varies in a non-linear way with respect to the exoskeleton pose (joint angles) and load.

The mounting errors influence the torque readings non-linearly with respect to the joint angle, while the non-axial torques depend in part on the interaction with human and in part on the dynamics and gravitational torques acting on the considered joint. For all the three sensors, the  $k_v$  constants have been experimentally evaluated. In order to minimize the effect of non-linear undesired term  $\delta\tau$ , an ANN has been used. ANN is a mathematical approximation approach that is capable to infer non-linear behavior from experimental acquisitions. The ANN with 7 neurons in the hidden layer and sigmoid activation function are deputed to estimate the error on the basis of the 4 angles and load on each axis. The angular information is useful to infer the assembly error component, whereas for the load influence the gravitational torque has been used.

To train the neural network the whole workspace has been partitioned in 414 target points. The torque sensor readings were acquired while the exoskeleton was holding the target position. For each joint, the training has been done using as input the 4 angles and the gravity torque that act on the joint (computed by model), and as output the residual value  $\delta\tau = G_i(\theta_m) - k_v * v$ , where  $G_i$  is the gravity load on the  $i$ -th joint when the pose is given by the angle vector  $\theta_m$ . The set of target points was divided in 3 parts: 70% for the training set, 20% for the validation set and 10% for the test set. The regression value between the ANN output and the target points is 0.99. The actual sensor torque estimation is given by  $\hat{\tau}_s = k_v * v + \delta\tau(\theta_m, G_i)$ , and a scheme of this estimation is shown in the Fig. 10.

### C. Control Hardware

The control architecture of the Rehab-Exos is decentralized and based on the EtherCAT communication bus in order to guarantee both optimal signal to noise ratio in the acquisition of analogical signals, i.e. force sensors, and higher standards of safety. The EtherCAT communication network consists of one

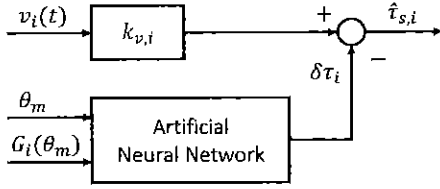


Fig. 10. The estimated sensor torque is obtained as the sum of sensor's reading and the predicted undesired non-linear term.

master controller and four Ethercat Slave Controllers (ESC), one for each actuation joint. The master controller is handled by Simulink Real-Time™ Operating System that executes the centralized control model at 2 kHz frequency.

Motors of the exoskeleton consist of three 170 VDC power supplied brushless motors on the 1st, 2nd and 4th joint, each one driven by programmable current driver and one 48 VDC power supplied DC motor on the 3rd joint. All of them are provided with one incremental encoder and one torque sensor.

Each ESC board is a custom control board featuring an up to 72 Mhz ARM7 micro-controller, 4 14-bit DAC output interfaces (to set the reference of the current drives), 10 14-bit Analog-to-Digital Converter (ADC) channels (to acquire the torque signals through 2 Wheatstone full-bridge channels that are pre-amplified) and the EtherCAT ET1100 controller linking to double-port Ethernet interface.

### III. DYNAMIC MODEL

#### A. Single joint model

The joints of the exoskeleton can be modeled with a lumped parameter model due to the elasticity of the harmonic drive speed reducer and torque sensor (for joints 1, 2, and 4) and of tendon transmission for joint 3. The used single joint model is a 2-mass with spring and damper (Fig. 11).

The single joint dynamics is formulated by the following equations:

$$J_{m,i}\ddot{\theta}_{m,i} + c_{m,i}\dot{\theta}_{m,i} + c_{t,i}(\dot{\theta}_{m,i} - \dot{\theta}_{j,i}) + k_{t,i}(\theta_{m,i} - \theta_{j,i}) = \tau_{m,i} + \tau_{d,i}$$

$$J_{l,i}\ddot{\theta}_{j,i} + c_{t,i}(\dot{\theta}_{j,i} - \dot{\theta}_{m,i}) + k_{t,i}(\theta_{j,i} - \theta_{m,i}) = \tau_{l,i} \quad (7)$$

where referring to the  $i$ -th joint,  $\theta_{m,i}$  and  $\theta_{j,i}$  stand for motor and joint angles respectively,  $k_{t,i}$  and  $c_{t,i}$  are the stiffness and viscous coefficient of the transmission, that were experimentally characterized.  $J_{m,i}$  is motor inertia,  $J_{l,i}$  is average link inertia considered as constant,  $\tau_{m,i}$  is the motor torque,  $\tau_{d,i}$  is a disturbance torque acting on the motor rotor which accounts for internal friction and ripple effects of both motor and harmonic drive, while  $\tau_{l,i}$  is the external torque acting directly on the output link. The  $\tau_{l,i}$  torque accounts for the exogenous input due to the interaction with the human, and endogenous input accounting for unmodeled non-linear effects, such as dynamic or gravity forces.

1) *Experimental characterization of single joint performance:* As described in II-A the joint is equipped with a torque sensor that is a part of the transmission chain and is capable of measuring the elastic torque  $\tau_{s,i}$ , which acts between motor rotor and joint output link. The elastic sensor torque can be expressed by  $\tau_{s,i} = k_{t,i}(\theta_{j,i} - \theta_{m,i})$ . The

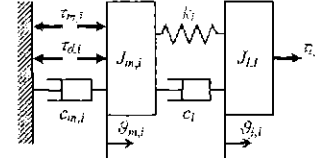


Fig. 11. The 2-mass model for each joint

no period... did you want to say more?

TABLE V  
THE NATURAL FREQUENCY OF THE JOINTS

Joint	Avg. link inertia [Kg/m <sup>2</sup> ]	Natural freq. [Hz]
1	0.9639	19.3930
2	1.11	18.3501
4	0.1925	39.6797

joint dynamics can be re-written expliciting the  $\tau_{s,i}$  readings starting from  $\tau_{s,i}$  definition, its 1st and 2nd derivatives and using the equations 7. It is obtained:

$$\ddot{\tau}_{s,i} + \frac{c_{t,i}}{J_i} \dot{\tau}_{s,i} + \frac{k_{t,i}}{J_i} \tau_{s,i} = \frac{k_{t,i}}{J_{l,i}} \tau_l + \frac{k_{t,i}}{J_{l,i}} \tau_g - \frac{k_{t,i}}{J_{m,i}} \tau_d - \frac{k_{t,i}}{J_{m,i}} \tau_m \quad (8)$$

where  $J_i = J_l J_m / (J_l + J_m)$ . The natural frequency of this system is  $\omega_n = \sqrt{k_{t,i}/J_i}/2\pi$ . The natural frequency has been experimentally evaluated for a single joint in a test-rig analyzing the response of the  $\tau_s$  when a chirp command is used for the  $\tau_m$  motor torque.

From Fig. 11 use of the Half-Power Bandwidth method returns  $c = 11.8 \text{ Nms/rad}$  as the overall damping coefficient of the flexible joint (this value has also been validated via the Logarithmic Decrement method). Considering the exoskeleton,

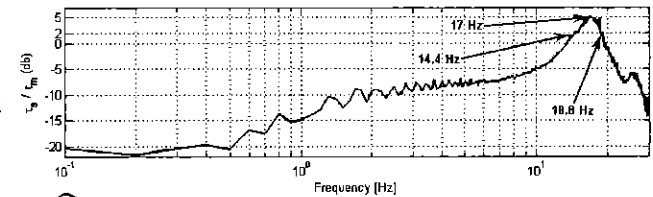


Fig. 12. Experimental open-loop response (Bode magnitude plot) of joints 1, 2 and 4) joint sensor torque vs. motor torque command.

Do they all have the same curve? Why? every joint sees a link inertia that depends on the pose so the natural frequency of each joint depends on the pose of the exoskeleton. Considering an average link inertia, it can be obtained the natural frequency for each joint elastic transmission. Results are shown in the TABLE V. For all these three joints the motor inertia is the same and it is equivalent to 3.742 Kg/m<sup>2</sup>

#### B. Multiple joints model

Given the single joint two-mass model, the dynamic model of the whole exoskeleton can be formulated in matrix form as follows:

$$\begin{cases} J_m D\ddot{\theta}_m + B_m D\dot{\theta}_m + C_t(D\dot{\theta}_m - \dot{\theta}_j) + K_t(D\theta_m - \theta_j) = \\ \tau_m + \tau_d \\ M(\theta_j)\ddot{\theta}_j + C(\dot{\theta}_j, \theta_j)\dot{\theta}_j + C_t(\dot{\theta}_j - D\dot{\theta}_m) + K_t(\theta_j - D\theta_m) + \\ + G(\theta_j) = J^T F_h \end{cases} \quad (9)$$

where  $J_m$ ,  $B_m$ ,  $D$ ,  $K_t$  and  $C_t$  are diagonal matrices.  $J_m$  and  $B_m$  model inertia and viscous friction at motor respectively, while  $K_t$  and  $C_t$  model stiffness and damping associated to the elastic transmission and  $D$  models the transmission reduction factor introduced by joint gearheads;  $G$  models the effects of gravity force on links.  $F_h$  are the external forces acting on the system due to human interaction and the respective joint torques are computed by multiplying them by the transposed Jacobian matrix  $J^T$  evaluated in the actual exoskeleton configuration. The multi-joint model introduces cross-coupling among joints and non-linearities, with terms  $C(\dot{\theta}_j, \theta_j)$  that models Coriolis effects and  $M(\theta_j)$  that represents links inertia.

By taking into account that the real dynamics has terms  $M(\theta_j)$  and  $C(\dot{\theta}_j, \theta_j)$  depending on the actual joint configuration, the first term can be decoupled into a diagonal constant component and a variable component as follows:

$$M\ddot{\theta}_j = \bar{M}\ddot{\theta}_j + \Delta M(\theta_j)\ddot{\theta}_j \quad (10)$$

and introducing the following variable substitution for joint torque  $\tau_s$

$$\begin{cases} \tau_s = -K_t(D\theta_m - \theta_j) \\ \dot{\tau}_s = -K_t(D\dot{\theta}_m - \dot{\theta}_j) \\ \ddot{\tau}_s = -K_t(D\ddot{\theta}_m - \ddot{\theta}_j) \end{cases} \quad (11)$$

the dynamics equations can be reformulated as follows:

$$\begin{cases} J_m D\ddot{\theta}_m + B_m D\dot{\theta}_m = K_t^{-1} C_t \dot{\tau}_s + \tau_s + u + \tau_d \\ \ddot{\tau}_s + C_t J_i^{-1} \dot{\tau}_s + K_t J_i^{-1} \tau_s = K_t J_m^{-1} B_m D\dot{\theta}_m + \\ + \bar{M}^{-1} K_t J^T F_h - K_t J_m^{-1} \tau_d - K_t J_m^{-1} u \end{cases} \quad (12)$$

where  $u$  represents the actual control command and the external disturbance forces have been collected within the external load force  $F_h$  term (see Appendix I for detailed derivation of terms).

This form of the dynamics equation is useful for defining a full-state feedback control law and an optimal observer for the estimation of joint torque.

1) *Joint acceleration estimation*: The full dynamics model of the exoskeleton is dependent on the acceleration of each joint. In order to estimate and compensate for the dynamics of the device, an observer for the joint acceleration has been designed. The observer estimates the acceleration from motor encoder  $\theta_{m,i}$ , joint torque  $\tau_{s,i}$  and the imposed control torque  $\tau_{m,i}$ .  $\tau_{s,i}$  is the torque measured by the sensor at the joint and can be expressed as in equation (12).

The acceleration can be estimated starting from a model of the actuation group (motor and gearhead), in particular by modeling the torque acting on the actuation group as  $\tau_{m,i} - \tau_{s,i}$  and by considering the losses as a static and a velocity-dependent viscous friction. Thus, the acceleration can be estimated as:

$$\begin{cases} \ddot{\theta}_{m,i} = 0 & \text{for } -\tau_{A,i} < \tau_{m,i} - \tau_{s,i} < \tau_{A,i} \\ \ddot{\theta}_{m,i} = \frac{\tau_{m,i} - \tau_{s,i} - c_{m,i}\dot{\theta}_{m,i}}{J_{m,i}} & \text{otherwise} \end{cases} \quad (13)$$

where  $\tau_{A,i}$  is the static friction torque and  $c_{m,i}$  is the dynamic friction coefficient that were experimentally evaluated. The torque saturation effects due to power supply voltage limits are modeled as:

$$k_c \frac{-V_{max} - k_v \dot{\theta}_{m,i}}{R} < \tau_{m,i} < k_c \frac{V_{max} - k_v \dot{\theta}_{m,i}}{R} \quad (14)$$

depending on the electric constants of each motor, and in particular where  $k_c$  is the associated torque constant,  $k_v$  is the velocity constant,  $R$  is the winding terminal resistance and  $V_{max}$  is the maximum supply voltage to the motor. An optimum Kalman observer has been used to estimate the acceleration term  $\ddot{\theta}_{m,i}$  and a diagram of the estimation of acceleration by using control and measured torques is shown in Fig. 13.

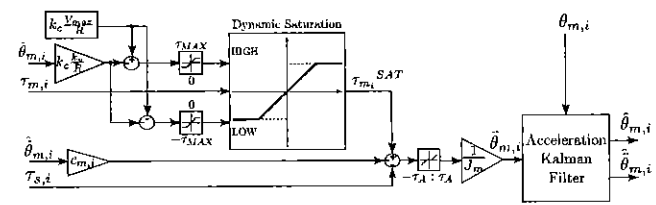


Fig. 13. Estimation of the acceleration from torque measurement

The model can be expressed in the state variable form as follows:

$$\begin{cases} \dot{x} = Ax + \Gamma d \\ y = Cx \end{cases} \quad (15)$$

where

$$x = \begin{bmatrix} \theta_{m,i} \\ \dot{\theta}_{m,i} \\ \ddot{\theta}_{m,i} \end{bmatrix} \quad A = \begin{pmatrix} 0 & 1 & 0 \\ 0 & 0 & 1 \\ 0 & 0 & 0 \end{pmatrix} \quad \Gamma = \begin{bmatrix} 0 \\ 0 \\ 1 \end{bmatrix} \quad C = \begin{pmatrix} 1 & 0 & 0 \\ 0 & 0 & 1 \end{pmatrix} \quad (16)$$

and  $d$  is the process noise.

The observer can be formulated as:

$$\dot{\hat{x}} = A\hat{x} + L(y - C\hat{x}) \quad (17)$$

where  $L$  is the gain matrix of the observer. A scheme of the observer is depicted in figure (14). *why different format?*

As an example, the comparison between the real-time estimated acceleration (red dotted line) and the off-line calculated acceleration (blue solid line) for the first two joints is shown in figure 15.

2) *Dynamics compensation*: As reported by equation (38), the torques measured by joint sensors are due to the human force and any load applied on the links ( $F_l$ ). To have a good estimation of human forces by torque sensors, it is necessary to remove from torque measurements the gravity and dynamics

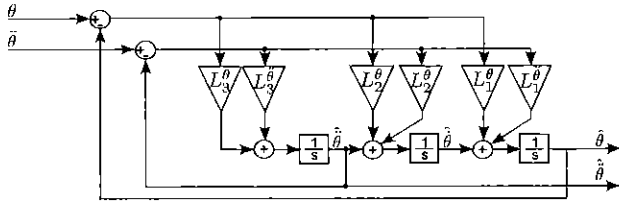


Fig. 14. Block diagram of the acceleration observer

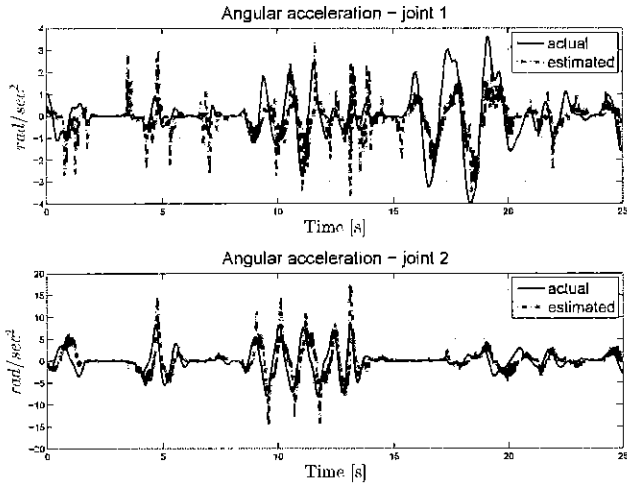


Fig. 15. Comparison between the estimated and actual acceleration

loads applied to the links. The gravity contribution depends only on the pose of the exoskeleton and it can be calculated by the position signals provided by the motor encoders. The gravitational term is already compensated in feed-forward by the term  $\hat{G}(\hat{D}\hat{\theta}_m)$  in  $\tau_m$ , except for the term  $\delta g$ . On the other side, the dynamics contribution depends both on the pose and the acceleration and velocity of the links, which are not directly provided by any sensor, but are provided in first approximation as  $D\hat{\theta}_m$  by the observer described in section III-B1.

The dynamics/torques due to the links inertia and measured by the joint torque sensors can be so estimated as the sum of the inertial contribution and the Coriolis effect:

$$\hat{\tau}_{dyn} \approx \hat{M}(D\hat{\theta}_m)D\ddot{\theta}_m + \hat{C}(D\hat{\theta}_m, D\dot{\theta}_m)D\dot{\theta}_m \quad (18)$$

where matrices  $\hat{M}$  and  $\hat{C}$  are calculated taking into account for each joint the inertia of the parts supported by the torque sensor, discarding the inertia of the actuator of the joint.

The estimated dynamic torques are then used to compensate the dynamic effects of the link: the compensation torques  $\alpha\hat{\tau}_{dyn}$ , with  $0 < \alpha < 1$ , are a percentage of the estimated torques  $\hat{\tau}_{dyn}$ . The compensation torques are added to the desired torques  $\tau_s^D$  as input to the state feedback controller and feed-back with the estimated torque  $\hat{\tau}_s$ .

#### IV. FULL STATE, BASIC AND PASSIVITY-BASED FEEDBACK CONTROLLERS

From the full dynamic model of the exoskeleton, a novel full state feedback control law was derived and implemented. This control law is identified in the following with the acronym JTFC1 and explained in subsection IV-B. To implement the control, the state of the system and, more in particular, the joint torque was estimated through a Kalman Filter described in subsection IV-A. To evaluate the performance of the proposed full state feedback control, two other torque controls inspired to existing joint torque controls available in literature have been implemented, identified respectively with the acronyms JTFC2 and JTFC3.

The JTFC2, presented in subsection IV-C, is based on a torque control for single joint based on torque sensor first introduced by Hashimoto [31]. In order to compare the basic torque control with our full state feedback control, the Hashimoto formulation was extended and generalized to a multi-dof case.

The JTFC3, reported in subsection IV-D, was inspired to the passivity-based control law [32] implemented for the DLR Light Weight Robot III (LWR III) that guarantees the passivity of the controlled system. The DLR LWR III shows a joint design compatible with the Rehab-Exos one, since both systems make use of the joint torque sensor to estimate the interaction torques/forces with the environment/human.

##### A. An optimal observer for estimation of joint torque

Since the correct state estimation is essential for the design of a full-state feedback joint-torque controller, the knowledge of the interaction torques between the human arm and the exoskeleton are required for torque control implementation. The joint torque sensor provides a raw measurement  $\tau_{s,i}$  that can be used together with the measured joint position  $\theta_{m,i}$  to filter the sensed torque and to estimate the full system state, given by  $[\tau_{s,i}, \dot{\tau}_{s,i}, \theta_{m,i}, \dot{\theta}_{m,i}, \tau_{d,i}, \tau_{l,i}]$ , where  $\tau_l = J^T F_l$ . Thus, a full-state Kalman filter has been designed to clean out both  $\theta_{m,i}$  from quantization noise  $w_{\theta,i}$  and  $\tau_{s,i}$  from measurement noise  $w_{\tau,i}$ , as well as to estimate the remaining variables.

Following [33], the dynamics of the two state components  $\tau_{d,i}$  and  $\tau_{l,i}$  can be modeled as two distinct Wiener processes (i.e. as two distinct non-stationary random processes)  $\dot{\tau}_{d,i} = v_{d,i}$  and  $\dot{\tau}_{l,i} = v_{l,i}$ . Starting from equations (43,44) the following meta-system can be derived:

$$\begin{cases} \dot{\tau}_i = A_i \tau_i + B_i \tau_{m,i} + \Gamma v_i \\ y_i = C \tau_i + w_i \end{cases} \quad (19)$$

where  $\tau_i^T = [\dot{\tau}_{s,i}, \tau_{s,i}, \dot{\theta}_{m,i}, \theta_{m,i}, \tau_{l,i}, \tau_{d,i}]$  is the meta-state vector,  $v_i^T = [v_{l,i}, v_{d,i}]$  is the vector of process noises with



variances  $V_{l,i}$  and  $V_{d,i}$ ,  $w_i^T = [w_{\tau,i} \ w_{\theta,i}]$  is the vector of measurement noises with variances  $W_{l,i}$  and  $W_{d,i}$ , whereas:

$$A_i = \begin{pmatrix} \frac{-c_{t,i}}{J_i} & \frac{-k_{t,i}}{J_i} & \frac{k_{t,i}b_{m,i}}{J_{m,i}} & 0 & \frac{k_{t,i}}{J_{l,i}} & \frac{-k_{t,i}}{J_{m,i}} \\ 1 & 0 & 0 & 0 & 0 & 0 \\ \frac{c_{t,i}}{k_{t,i}J_{m,i}} & \frac{1}{J_{m,i}} & \frac{-b_{m,i}}{J_{m,i}} & 0 & 0 & \frac{1}{J_{m,i}} \\ 0 & 0 & 1 & 0 & 0 & 0 \\ 0 & 0 & 0 & 0 & 0 & 0 \\ 0 & 0 & 0 & 0 & 0 & 0 \end{pmatrix} \quad (20)$$

$$B_i = \begin{bmatrix} \frac{-k_{t,i}}{J_{m,i}} \\ 0 \\ \frac{1}{J_{m,i}} \\ 0 \\ 0 \\ 0 \end{bmatrix} \quad \Gamma = \begin{pmatrix} 0 & 0 \\ 0 & 0 \\ 0 & 0 \\ 0 & 0 \\ 1 & 0 \\ 0 & 1 \end{pmatrix} \quad C = \begin{pmatrix} 0 & 0 \\ 1 & 0 \\ 0 & 0 \\ 0 & 1 \\ 0 & 0 \\ 0 & 0 \end{pmatrix}$$

### B. A full state feedback controller (JTFC1)

The proposed control law is based on the full state obtained from the state observer described by (19) (20), where the input control  $u$  is splitted up into one term  $u_f$ , which implement control force behavior, and another term  $u_g$ , which acts as a gravity compensation

$$u = u_f + u_g \quad (21)$$

The two above terms are expressed as:

$$u_g = G(D\hat{\theta}_m) \quad (22)$$

$$u_f = -J_m K_t^{-1} \ddot{\tau}_s^D + B_m D\dot{\theta}_m + J_m \overline{M}^{-1} J^T \hat{F}_l - \hat{\tau}_d - J_i^{-1} J_m \tau_s^D + K_p e + K_d \dot{e} \quad (23)$$

where  $e = \tau_s - \tau_s^D$  is the error on sensor torque, given the desired sensor torque  $\tau_s^D$ . Let us assume moreover that  $\dot{\tau}^D = 0$  and  $\ddot{\tau}^D = 0$ , so that  $\dot{e} = \dot{\tau}_s$  and  $\ddot{e} = \ddot{\tau}_s$ , the expression (23) of  $u_f$  can be rewritten as

$$u_f = B_m D\dot{\theta}_m + J_m \overline{M}^{-1} J^T \hat{F}_l - J_i^{-1} J_m \tau_s^D - \hat{\tau}_d + K_p e + K_d \dot{e} \quad (24)$$

The modified dynamics with the control laws (21), (22) and (24), leads to a stable error dynamics equations:

$$\ddot{\theta}_m = \ddot{\theta}_j - K_t^{-1} \ddot{e} \quad (25)$$

$$0 = \ddot{e} + (C_t J_i^{-1} + K_d K_t J_m^{-1}) \dot{e} + (K_t J_i^{-1} + K_p K_t J_m^{-1}) e \quad (26)$$

The convergence of error  $e$  to zero can so be adjusted by choosing the proportional and derivative gains  $K_p$  and  $K_d$ , to obtain the desired dynamic response.

Figure 16 reports the schema of the proposed full state feedback control that takes into account the dynamic compensation contributes. Note that the torque sensor reads  $\tau_{s,i}$  and the commanded motor torques  $\tau_{m,i}$  are net of the gravity compensation term  $u_g$ .

Preprint submitted to IEEE Transactions on Robotics. Received: November 1, 2018 05:27:50 PST

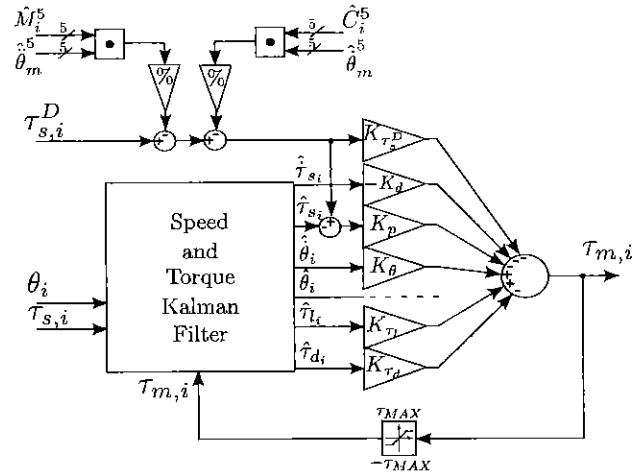


Fig. 16. The schema of the full state control feedback with the dynamic compensation.

### C. A basic state feedback controller (JTFC2)

The basic state feedback controller is derived assuming the following full model dynamics (extended the one introduced for a single joint by Hashimoto [31]), that differs from (9) for the absence of external forces:

$$\begin{cases} J_m D\ddot{\theta}_m + K_t(D\theta_m - \theta_j) = \tau_m + \tau_d \\ M(\theta_j)\ddot{\theta}_j + C(\dot{\theta}_j, \theta_j)\dot{\theta}_j + K_t(\theta_j - D\theta_m) + G(\theta_j) = J^T F_h \end{cases} \quad (27)$$

$$\tau_s = -K_t(D\theta_m - \theta_j) \quad (28)$$

Assuming the above full model dynamics, the input control  $u$  is designed as in (21), where for  $u_g$  is used (22).

The basic control law used in [31] can be generalized in case of multi-joint robot. Thus, according to the proposed notation, if one assumes  $e = \tau_s - \tau_s^D$  as the error on sensor torque, given the desired sensor torque  $\tau_s^D$ , and one assume moreover that  $\dot{\tau}^D = 0$  and  $\ddot{\tau}^D = 0$ , so that  $\dot{e} = \dot{\tau}_s$  and  $\ddot{e} = \ddot{\tau}_s$ , the control law can be written as

$$u_f = -J_i^{-1} J_m \tau_s^D + J_m K_t^{-1} K_d \dot{e} + J_m K_t^{-1} K_p e \quad (29)$$

The modified dynamics with the control law (29), leads to the following error dynamics equations:

$$\ddot{\theta}_m = D^{-1} \ddot{\theta}_l - D^{-1} K_t^{-1} \ddot{e} \quad (30)$$

$$J^T F_l - K_t J_m^{-1} \tau_d = \ddot{e} + K_d \dot{e} + (K_p + J_i^{-1} K_t) e \quad (31)$$

### D. A passivity-based feedback controller (JTFC3)

The passivity-based state feedback is derived assuming the following full model dynamics (introduced by Ott in [32]),

that differs from (9) for the absence of the motor's viscous friction term:

$$\begin{cases} J_m D\ddot{\theta}_m + C_t(D\dot{\theta}_m - \dot{\theta}_j) + K_t(D\theta_m - \theta_j) = \tau_m \\ M(\theta_j)\ddot{\theta}_j + C(\dot{\theta}_j, \theta_j)\dot{\theta}_j + C_t(\dot{\theta}_j - D\dot{\theta}_m) + G(\theta_j) + \\ + K(\theta_j - D\theta_m) = J^T F_h \end{cases} \quad (32)$$

$$\tau_s = -K_t(D\theta_m - \theta_j) \quad (33)$$

In [32] the control law  $u$  is designed as in (21) where  $u_g$  are the torques due to the gravity. For this work  $u_g$  is calculated as in (22). Whereas, the term  $u_f$  after some algebraic transformations can be written as:

$$u_f = -\tau_s^D + (J_m J_\theta^{-1} - I)B_m K_t^{-1} \dot{e} + (J_m J_\theta^{-1} - I)e \quad (34)$$

The modified dynamics within the control law (34), leads to the following error dynamics equations:

$$\begin{aligned} \ddot{\theta}_m &= D^{-1}\ddot{\theta}_j - D^{-1}K_t^{-1}\ddot{e} \\ K_t M^{-1}(\theta_j)(-\tau_s^D + J^T F_t) &= \\ \ddot{e} + (J_i^{-1} + B_m^{-1}M^{-1}(\theta_j)B_m + K_d K_t J_i^{-1})\dot{e} + \\ + (K_t J_i^{-1} + K_t M^{-1}(\theta_j) + K_p K_t J_i^{-1})e \end{aligned}$$

#### E. Impedance control / haptic rendering

The three torque control laws are used as inner feedback loop of the impedance control used to test the exoskeleton in the haptic rendering task. The desired end-effector force  $F_{ee}^D$  is due to the interaction with the virtual environment impedance. More in detail, the desired force is defined by:

$$\begin{cases} F_{ee}^D = 0, & x < x_d \\ F_{ee}^D = K_x(x - x_d) - D_x \dot{x}, & x \geq x_d \end{cases} \quad (35)$$

where  $x$  is the coordinate along the normal axis to the surface,  $x_d$  is the wall coordinate,  $K_x$  and  $D_x$  are the desired stiffness and damping respectively of the simulated virtual environment.

#### V. EXPERIMENTS AND RESULTS

The performance of the torque and impedance controls have been assessed by experimental tests. The tests show how the torque controls behave in constant and varying desired torque tracking. The first one is the transparency test in which the robot tries to keep the joint torque at zero Nm while the user is moving the exoskeleton. The second test is the haptic rendering with a slanted flat surface with different simulated stiffness. More details on each test are reported in the subsections below.

The implemented control laws (24), (29) and (34) have been set using the model parameters. The proportional and derivative PD gains ( $K_p$  and  $K_d$ ) have been chosen to obtain a desired error dynamics, *more in detail* the form that guarantees the minimum ITAE index. Notice that the control laws (24) and (29) have two degrees of freedom, i.e.  $K_p$  and  $K_d$  can be independently chosen, whereas the control law (34) exhibits a 1 degree of freedom, thus the two control gains are linked and they are calculated as a function of the desired inertia  $J_\theta$ .

#### A. Transparency

For the transparency test, two kinds of trials have been done. The first type of trial uses the JTFC1 control law described in the subsection IV-B in order to verify how much the dynamics compensations improve the desired torque tracking. The second type of trials are useful to compare the three control laws and to understand how the terms of the control inputs are related to the desired torque tracking. During the transparency tests the user has been linked with the exoskeleton in 2 points: the arm in order to transmit the shoulder movement, and the forearm in order to exchange the elbow movement.

In order to validate the interaction torque control and to evaluate the torque tracking performance, an additional force sensor has been mounted on the end-effector of the exoskeleton to measure the actual forces  $F_h^*$  applied by the user. As transparency index the measured end effector norm force and the reflected torques at the joints have been used. The reflected torques at the joint are calculated as  $\tau_s^* = J^T F_h^*$  and then compared to the interaction torques estimated by the optimal observer.

1) *How dynamic compensation affects the transparency:* In order to understand how the dynamic compensation affects the transparency, the scheme of figure 16 has been implemented *using* that uses the JTFC1 control law plus the dynamics terms multiplied by  $\alpha$ , with  $0 \leq \alpha \leq 1$ .

The experimental results for torque tracking, with a desired torque  $\tau_s^D = 0$ , are shown for the second joint  $J_2$  in Fig. 17, that is the joint with the highest link inertia. A user has moved *without constraints the exoskeleton* grabbing the force sensor mounted at the end effector. The control was set to follow his movement at zero-torque without (Fig. 17(a)) and with (Fig. 17(b)) dynamics compensation.

The upper plots show the joint position (blue solid line) and acceleration (red dotted line), to demonstrate the movements were similar in both cases. The lower plots represent the interaction torques estimated by the observer (blue solid line) and measured by the force sensor (red dotted line). Even if the estimated torques are similar in both cases, with dynamics compensation the actual interaction forces are lower, demonstrating that torque tracking is more precise and the user has to compensate less for the link dynamics.

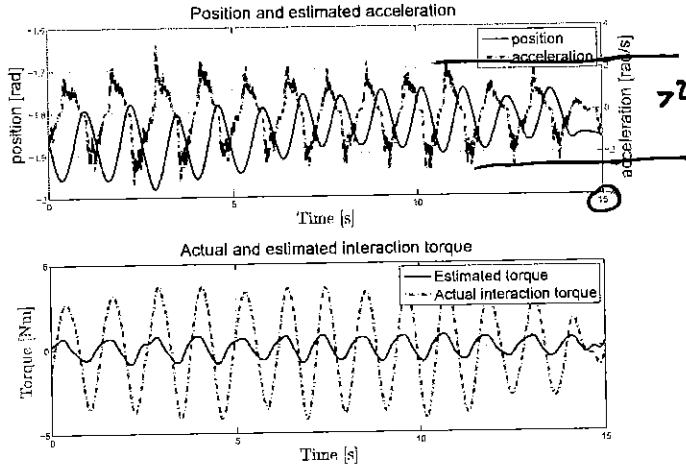
2) *Comparison between the three torque controllers JTFC1, JTFC2 and JTFC3:* For this kind of trials the three joint torque controls presented in the section IV were tested with a desired torque set to zero ( $\tau_s^D = 0$ ) as for the trials in the subsection V-A1.

In order to have comparable results and repeatability of trials, the transparency of the exoskeleton was tested with the same subject while he was trying to perform the same circular trajectory at the end effector, with the same velocity using the three different controls. The subject had visual cue (a circle of 150 mm of radius) while performing the task. To evaluate the transparency performances only data in the same range of speed were used. Despite the user tried to track the desired trajectory, the executed ones and their speeds were somehow influenced by the used torque control. The average speed at

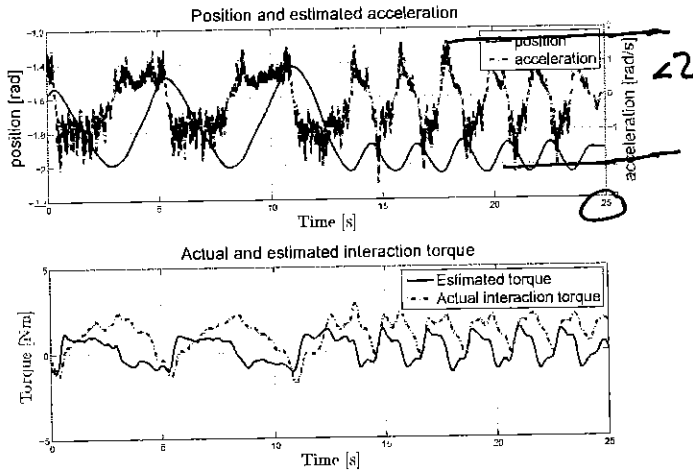
less clear from Fig 17 due to different axes scaling + different movements.

specifically

awkward reword.



(a) Without dynamics compensation



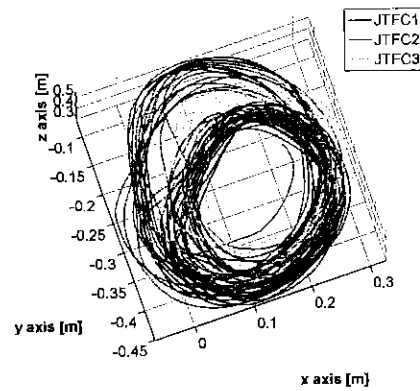
(b) With dynamics compensation

Fig. 17. Comparison between the measured torque  $\tau_s$  and calculated torque by force sensorTABLE VI  
MEAN AND STD. DEV. OF THE E.E. SPEED IN THE TRANSPARENCY EXPERIMENTS

Control	Avg. speed [m/s]	Std. dev. [m/s]
JTFC1	0.4198	0.0810
JTFC2	0.4460	0.1374
JTFC3	0.3867	0.1213

the end effector of the three controls are listed in the TABLE VI. The real trajectories can be shown in the Fig. 18.

As the reader can see, the red trajectories (the ones obtained by using the control JTFC2) are less accurate due to the limited torque control performance. Moreover, from the analysis of the control torque errors at the joints (Fig. 19), it can be seen that the control JTFC2 exhibits an average error that is independent from the link inertia. The torque error over link inertia ratio for the elbow joint is the highest and this leads to a greater disturbance on the fine trajectory execution. The average force measured at the end effector are shown in Fig. 20.



where's the target circle?

Fig. 18. The trajectories performed during the transparency test using the three control laws.

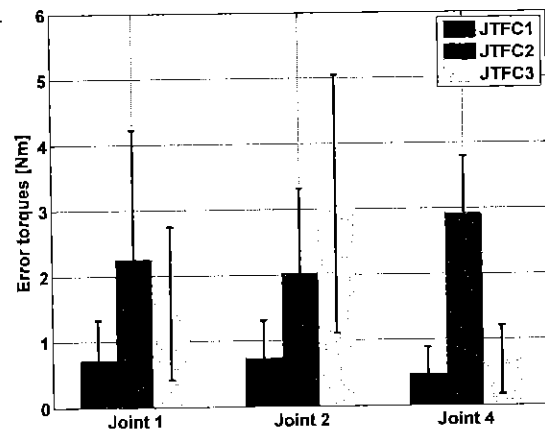


Fig. 19. The torque errors of the 3 controllers for joints 1, 2 and 4.

The value of the end-effector forces provides an overall index of the exoskeleton transparency with a given torque control (when  $\tau_s^D = 0$ ). The control JTFC1 that implements a full-state feedback control performs better because it models in a more accurate and general way the joint dynamics. Moreover, the control JTFC1 compensates for the modeled effects. Notice that, at joint level, the control JTFC3 behaves more similar to JTFC1 rather than to the control JTFC2, in fact the torque errors of the control JTFC1 and JTFC3 seems to be correlated to the link inertia.

### B. Haptic rendering

The implemented torque controls can be used to render the interaction forces exchanged with a virtual surface of a given stiffness and damping, acting as impedance controls. In these tests the contact forces at the end-effector are proportional to the penetration length of the end-effector into the virtual wall surface and to its speed. The force is then converted to desired torques at the joints by multiplying the equation defined in (35) by the transpose of the Jacobian, where the equations

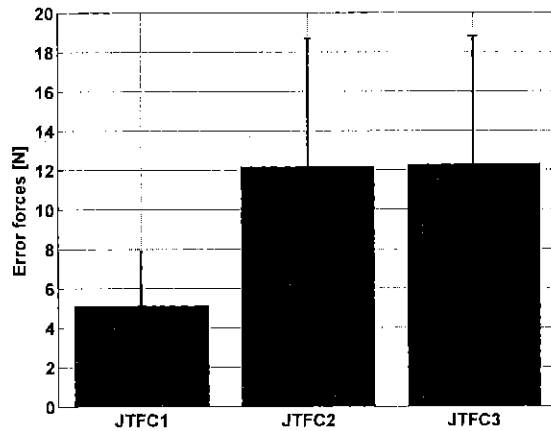


Fig. 20. The force error at the end effector of the 3 controllers.

(24), (29) and (34) have been used respectively for JTFC1, JTFC2 and JTFC3.

In the experiments the user grabs the exoskeleton only at the end effector without applying any other force on the links. In this way, the forces measured by the end-effector's force sensor have been used to evaluate the overall system performance since these forces are not involved for the torque control.

The rendering experiments were composed by four different type of trials as depicted in Fig. 21:

- T1: "Slide on surface" experiment with moderate forces;
- T2: "Slide on surface" experiment with high forces;
- T3: "Collision with a surface" experiment with moderate speed;
- T4: "Collision with a surface" experiment with high speed.

During the T1 and T2 trials the experimenter slid the end-effector on the surface without sudden variations of penetration. The difference between the T1 and T2 trials is the average level of force along the orthogonal axes at the surface. In the T3 and T4 trials the aim is to test the dynamic performance of the controls, so the experimenter pushed the end-effector on the surface. The difference between the T3 and T4 trials is the average slope of the desired force profiles. The 4 tests have been evaluated for each controls and with three different environment parameters, in order to consider a low, an intermediate and a high stiff wall.

The TABLE VII reports the three environment parameters, the average forces involved in the T1 and T2 trials, the average force peaks and the average slope of the T3 and T4 trials.

To evaluate the performances of the three different torque controls three indexes have been proposed, i.e.

- the mean of the norm of the error force vectors;
- the mean of the absolute value of the error of the orthogonal component;
- the mean of the angle between the desired forces and the measured ones.

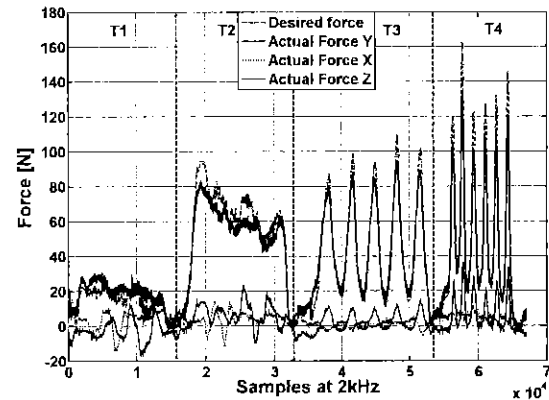


Fig. 21. The four trial types during an haptic rendering test. The desired forces is plotted with red dashed lines, the measured orthogonal forces are plotted with blue solid lines while the two tangential components are with magenta and black solid lines.

TABLE VII  
THE AVERAGE FORCES INVOLVED IN THE T1 AND T2 TRIALS, THE AVERAGE FORCE PEAKS AND THE AVERAGE SLOPE OF THE T3 AND T4 TRIALS.

Env. Params.	T1	T2	T3	T4
5 kN/m	22.22 N	50.79 N	83.33 N	112.33 N
2 Ns/m	-	-	127.28 N/s	518.49 N/s
20 kN/m	22.81 N	66.14 N	103.97 N	136.97 N
7 Ns/m	-	-	159.25 N/s	550.99 N/s
40 kN/m	24.98 N	59.37 N	88.32 N	126.20 N
10 Ns/m	-	-	120.39 N/s	616.03 N/s

The results can be shown in the Fig. 22. The first graph shows the average difference between the rendered forces by the controls and the desired forces with an aggregate index, i.e. the norm of the error vector. From this graph the reader can see that in all the condition the JTFC1 control performs better than the others, in fact the mean of the error is around 10 N in all the three cases.

To decompose the informations given in the first graph, other two indexes are considered, that are the average error of the orthogonal component of the force and the angle between the desired and the rendered forces. Unlike the norm of the error vector, these two indexes give information on the amplitude and the direction of the undesired force components. The second graph highlights that the JTFC1 control leads to an average error of 5 N along the task direction independently from the environment parameters, that is a good result coupled with the exhibited stable contact with the surface in every condition. The third graph is substantially in agreement with the previous ones.

## VI. DISCUSSION

The results highlight the advantages of using a full-state feedback controller that compensates also for estimated disturbance torques and for viscous torque losses of the motor. The major benefit on the use of the full state feedback



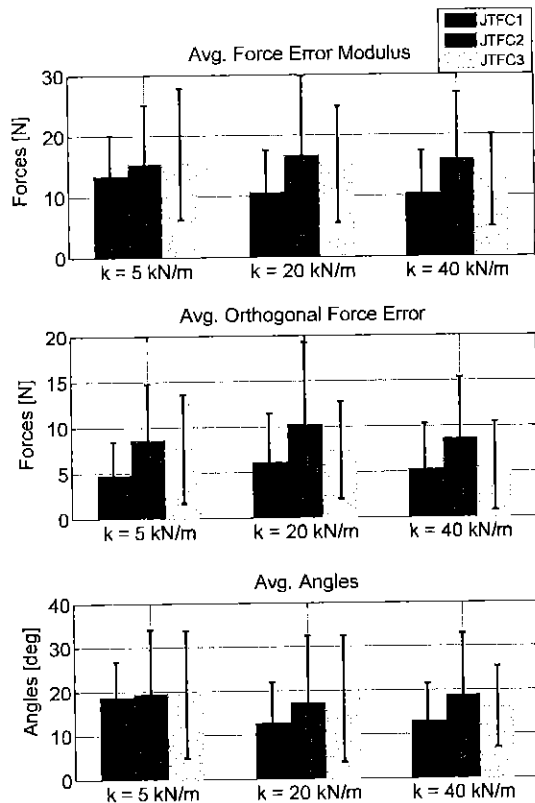


Fig. 22. At the top, the average of the modulus of the error force vectors at the end effector of the 3 controllers in the rendering task. For this test, 3 stiffness has been evaluated: 5kN/m (small), 20 kN/m (medium) and 40 kN/m (high). In the middle, the average error forces of the orthogonal component. At the bottom, the average angle between the desired force vectors and the measured ones.

control is high exhibited transparency during the free motion task. This means that the exoskeleton can affect less the user desired motion and at the same time the robot is able to more accurately identify the user intention (the human forces/torques).

Although the basic state feedback control (JTFC2) presents an average force modulus at the end-effector similar to the passivity-based feedback control (JTFC3), it hinders the user voluntary motion more than the other controls do. In fact the end-effector trajectory due to the control JTFC2 is the farthest from the desired one. This is because the JTFC1 and the JTFC3 take into account (although different ways) both the link's inertia and the motor's inertia, whereas the JTFC2 control considers only the motor's inertia. The full state controller explicitly estimates the load torques and feed-forwards this contribution by multiplying it by a gain. On the other side, the passivity-based controller imposes by control the desired link's inertia, thus this is a direct objective of the control.

The high transparency (the average force modulus at the end-effector is less than 6 N for JTFC1) is also due to the effect

of the dynamic compensations. A correct estimation of the joint acceleration is crucial to obtain a transparency enhancement, this is the reason why the dynamic contributions are weighted by a constant less than 1. In fact only with a perfect acceleration estimation, it can be obtained a high transparency keeping a stable behavior. The proposed methodology for the estimation of the acceleration through torque sensor's data and motor's data can help to improve the acceleration calculation.

An important result is the wide range of stable impedances that the system can render. The Rehab-Exos was able to render a flat surface with a stiffness equal to 40 kN/m with all the three compared control laws with different performances but still preserving stability. This is certainly due to inherent mechanical damping of the system.

The mechanical design of the exoskeleton influences its performances. The residual torques at the joint are basically the effects of the unmodeled link inertia and the joint friction. A more light design made by small motors and small transmission ratio will lead to a more backdrivable solution ~~with~~ <sup>at</sup> the ~~price~~ <sup>cost</sup> of ~~a~~ less torque available at the joint. This could be a solution to experience an even more transparent device. Moreover the torque sensor requires a more robust design; more in detail, to obtain a smaller sensitivity to non-axial loads a spoke with wider beams can be implemented.

The choice of a joint with an active impedance by control based on a torque sensor presents a valid alternative to the passive inherent compliant actuators in order to achieve a more compact and simpler mechanics and electronics. The proposed torque control combined with the joint mechanics allow to build <sup>allow</sup> safe and responsive control strategies suitable for rehabilitation and assistance.

## VII. CONCLUSION

This paper presents the Rehab-Exos exoskeleton design and in particular the design of the joint torque sensors based on strain gauges. Some sensor's issue have been explained and two possible hypotheses have been proposed. Then an interaction torque control has been developed and validated by experimental tests such as the transparency test and the haptic interaction tasks. The kinematics and dynamics of the device are calculated by a full dynamics model implemented in a centralized torque control. The torque tracking for each joint is performed by single-joint full-state Kalman filter and a torque feedback controller. The centralized control provides to each single-joint observer the desired torque for force feedback and an estimation of the joint torques due to links dynamic loads to be compensated by the control as feed-forward contributions. The developed full-state feedback control was then compared with a basic feedback control and a passivity-based feedback control. Results show how the full-state approach is effective for estimating the human interaction force cleaned up of the inertial and gravity contributions due to the non negligible mechanical properties of the exoskeleton structure. The full-state feedback control is more accurate and transparent than the other two controls. The proposed control strategy combined with the presence of a joint torque sensor can enhance the performances of the human-robot interaction based on exoskeleton even in ~~the~~ <sup>the</sup> presence of non backdrivability.

or use ";"  
(semicolon)

allow  
building

awkward  
grammar

## ACKNOWLEDGMENTS

The authors would like to thank Marco Graffiedi for his contribute on the study of the torque sensor cross-talk reading.

## VIII. APPENDIX I

Let us study the effect under static condition of the application of a motor torque compensating for the non-linearity due to gravity, estimated as  $\hat{G}(D\hat{\theta}_m)$ , with:

$$\tau_m = \hat{G}(D\hat{\theta}_m) + u \quad (36)$$

where  $u$  represents the actual control command. Under static conditions it can be found that:

$$u = -J^T F_h + G(\theta_j) - \hat{G}(D\hat{\theta}_m) = -J^T F_h \quad (37)$$

since  $\hat{G}(D\hat{\theta}_m) \simeq G(\theta_j)$ . Under dynamic conditions, the incomplete cancellation of the gravity component due to the elasticity of the joint transmission can be modeled by introducing a disturbance term  $\delta g = G(\theta_j) - \hat{G}(D\hat{\theta}_m)$ , that can be summed up to  $F_h$  as a disturbance noise supported by the operator.

So a variable apparent dynamic force  $F_{dyn}$  can be defined such that  $J^T \Delta F_{dyn}(\dot{\theta}_j, \theta_j) = -\Delta M(\theta_j)\dot{\theta}_j - C(\dot{\theta}_j, \theta_j)\dot{\theta}_j$ . The new variable  $\Delta F_{dyn}$ , representing uncompensated and/or unmodeled dynamics, can be considered as a disturbance force and considered as a contribution term to the overall external load force  $F_l$  expressed by:

$$F_l = F_h + \delta g + \Delta F_{dyn} \quad (38)$$

This in general states that the external forces are the sum of exogenous  $F_h$  and endogenous inputs  $\delta g + \Delta F_{dyn}$ . While exogenous inputs are unknown a priori and depending on human operator behavior, endogenous inputs can be estimated and compensated to some extent.

So introducing the variable substitution expressed by (12), dynamic equations can be reformulated as follow:

$$J_m D\ddot{\theta}_m + B_m D\dot{\theta}_m = K_t^{-1} C_t \dot{\tau}_s + \tau_s + u + \tau_d \quad (39)$$

$$\bar{M}\ddot{\theta}_j + K_t^{-1} C_t \dot{\tau}_s + \tau_s = J^T F_l \quad (40)$$

But we know that

$$\begin{aligned} K_t^{-1} \dot{\tau}_s + D\ddot{\theta}_m &= \ddot{\theta}_j \\ K_t^{-1} \dot{\tau}_s + D\dot{\theta}_m &= \dot{\theta}_j \end{aligned} \quad (41)$$

Then making substitution of (41) in (40) to eliminate  $\theta_j$  and its higher order derivatives, we obtain:

$$\bar{M}D\ddot{\theta}_m + \bar{M}K_t^{-1} \dot{\tau}_s + K_t^{-1} C_t \dot{\tau}_s + \tau_s = J^T F_l \quad (42)$$

and then replacing  $D\ddot{\theta}_m = J_m^{-1} \{-B_m D\dot{\theta}_m + K_t^{-1} C_t \dot{\tau}_s + \tau_s + u + \tau_d\}$  and defining  $J_t^{-1} = \bar{M}^{-1} [I + \bar{M}J_m^{-1}]$ , dynamics equations can be put in the following form:

$$J_m D\ddot{\theta}_m + B_m D\dot{\theta}_m = K_t^{-1} C_t \dot{\tau}_s + \tau_s + u + \tau_d \quad (43)$$

$$\begin{aligned} \ddot{\tau}_s + C_t J_t^{-1} \dot{\tau}_s + K_t J_t^{-1} \tau_s &= K_t J_m^{-1} B_m D\dot{\theta}_m \\ &+ \bar{M}^{-1} K_t J^T F_l - K_t J_m^{-1} \tau_d - K_t J_m^{-1} u \end{aligned} \quad (44)$$

This form of the dynamics equation is useful for defining a full-state feedback control law and an optimal observer for the estimation of joint torque.

## REFERENCES

- [1] H. S. Lo and S. Q. Xie, "Exoskeleton robots for upper-limb rehabilitation: State of the art and future prospects," *Medical engineering & physics*, vol. 34, no. 3, pp. 261–268, 2012.
- [2] E. Pirondini, M. Coscia, S. Marcheschi, G. Roas, F. Salsedo, A. Frisoli, M. Bergamasco, and S. Micera, "Evaluation of the effects of the arm light exoskeleton on movement execution and muscle activities: a pilot study on healthy subjects," *Journal of neuroengineering and rehabilitation*, vol. 13, no. 1, p. 1, 2016.
- [3] M. J. Kim, W. Lee, J. Y. Choi, Y. S. Park, S. H. Park, G. Chung, K.-L. Han, I. S. Choi, I. H. Suh, Y. Choi *et al.*, "Powered upper-limb control using passivity-based nonlinear disturbance observer for unknown payload carrying applications," in *Robotics and Automation (ICRA), 2016 IEEE International Conference on*. IEEE, 2016, pp. 2340–2346.
- [4] D. Buongiorno, E. Sotgiu, D. Leonardis, S. Marcheschi, M. Solazzi, and A. Frisoli, "Wres: a novel 3dof wrist exoskeleton with tendon-driven differential transmission for neuro-rehabilitation and teleoperation," *IEEE Robotics and Automation Letters*, 2018.
- [5] J. Rebelo, T. Sednaoui, E. B. den Exter, T. Krueger, and A. Schiele, "Bilateral robot teleoperation: A wearable arm exoskeleton featuring an intuitive user interface," *IEEE Robotics & Automation Magazine*, vol. 21, no. 4, pp. 62–69, 2014.
- [6] M. Mihelj, T. Nef, and R. Riener, "Armin ii-7 dof rehabilitation robot: mechanics and kinematics," in *Robotics and Automation, 2007 IEEE International Conference on*. IEEE, 2007, pp. 4120–4125.
- [7] R. Vertechy, A. Frisoli, A. Dettoni, M. Solazzi, and M. Bergamasco, "Development of a new exoskeleton for upper limb rehabilitation," in *Rehabilitation Robotics, 2009. ICORR 2009. IEEE International Conference on*. IEEE, 2009, pp. 188–193.
- [8] C. Carignan, M. Liszka, and S. Roderick, "Design of an arm exoskeleton with scapula motion for shoulder rehabilitation," in *Advanced Robotics, 2005. ICAR'05. Proceedings., 12th International Conference on*. IEEE, 2005, pp. 524–531.
- [9] A. Frisoli, F. Salsedo, M. Bergamasco, B. Rossi, and M. Carbonecini, "A force-feedback exoskeleton for upper-limb rehabilitation in virtual reality," *Applied Bionics and Biomechanics*, vol. 6, no. 2, pp. 115–126, 2009.
- [10] J. C. Perry, J. Rosen, and S. Burns, "Upper-limb powered exoskeleton design," *Mechatronics, IEEE/ASME Transactions on*, vol. 12, no. 4, pp. 408–417, 2007.
- [11] P. Garrec, J. Friconeau, Y. Measson, and Y. Perrot, "Able, an innovative transparent exoskeleton for the upper-limb," in *Intelligent Robots and Systems, 2008. IROS 2008. IEEE/RSJ International Conference on*. IEEE, 2008, pp. 1483–1488.
- [12] N. G. Tsagarakis and D. G. Caldwell, "Development and control of a soft-actuated exoskeleton for use in physiotherapy and training," *Autonomous Robots*, vol. 15, no. 1, pp. 21–33, 2003.
- [13] J. Klein, S. Spencer, J. Allington, J. E. Bobrow, and D. J. Reinkensmeyer, "Optimization of a parallel shoulder mechanism to achieve a high-force, low-mass, robotic-arm exoskeleton," *Robotics, IEEE Transactions on*, vol. 26, no. 4, pp. 710–715, 2010.
- [14] B. Vanderborght, A. Albu-Schäffer, A. Bicchi, E. Burdet, D. G. Caldwell, R. Carloni, M. Catalano, O. Eiberger, W. Friedl, G. Ganesh *et al.*, "Variable impedance actuators: A review," *Robotics and autonomous systems*, vol. 61, no. 12, pp. 1601–1614, 2013.
- [15] N. L. Tagliamonte, F. Sergi, D. Accoto, G. Carpino, and E. Guglielmelli, "Double actuation architectures for rendering variable impedance in compliant robots: A review," *Mechatronics*, vol. 22, no. 8, pp. 1187–1203, 2012.
- [16] J. F. Veneman, R. Kuidhof, E. E. Hekman, R. Ekkelenkamp, E. H. Van Asseldonk, and H. Van Der Kooij, "Design and evaluation of the lopes exoskeleton robot for interactive gait rehabilitation," *IEEE Transactions on Neural Systems and Rehabilitation Engineering*, vol. 15, no. 3, pp. 379–386, 2007.